J. Fluid Mech. (1969), *vol.* 35, *part* 4, *pp.* 625–656
Printed in Great Britain

Experiments on the generation of small water waves by wind

By E. J. PLATE, P. C. CHANG

Colorado State University, Fort Collins, Colorado

AND G. M. HIDY

National Center for Atmospheric Research, Boulder, Colorado

(Received 23 April 1968)

The generation and growth of small water waves by a turbulent wind has been investigated in a laboratory channel. The evolution of these oscillations with fetch was traced from their inception with amplitudes in the micron range under conditions of steady air flow. The experiments revealed that the waves are generated at all air velocities in small bursts consisting of groups of waves of nearly constant frequency. After travelling for some distance downstream, these wavelets attain sufficient amplitude to become visible. For this condition, a wind speed critical to raise waves is well defined. After the first wavelets appear, two new stages of growth are identified at longer fetches if the air speed remains unchanged. In the first of these, the wave component associated with the spectral peak grows faster with fetch than any other part of the wave spectrum of the initial waves until its amplitude attains an upper limit consistent with Phillips's equilibrium range, which appears to be universal for wind waves on any body of water. If the air flow is not changed, then the frequency of this dominant wave remains constant with fetch up to equilibrium. This frequency tends to decrease, however, with increasing wind shear on the water. In the second stage of growth, only the energy of wave components with spectral densities lower than the equilibrium limit tend to increase with fetch so that the wave spectrum is maintained near equilibrium in the high-frequency range of the spectrum.

The origin of the first waves and the rate of their subsequent growth was examined in the light of possible generating mechanisms. There was no indication that they were produced by direct interaction of the water surface with the air turbulence. Neither could any significant feedback of the waves into the turbulence structure be detected. The growth of the waves was found to be in better agreement with theoretical predictions. Under the shearing action of the wind, the first waves were found to grow exponentially. The growth rates agreed with the estimates from the viscous shearing mechanism of Miles (1962*a*) to a fractional error of 61 % or less. A slight improvement was obtained with the viscous theory of Drake (1967) in which Miles' model is extended to include the effect of the drift current induced by the wind in the water. Since the magnitude of the water currents observed in the tunnel is very small, this improvement is not significant.

1. Introduction

It is currently accepted that water surface waves can be generated by a turbulent wind through a sequence of mechanisms elucidated by Phillips (1957) and Miles (1962*a*). According to Phillips, the initial wavelets derive from resonance between the free modes of the water surface and the pressure field of the turbulent motion in the air flow. This class of water waves is predicted to grow linearly with time (or with fetch), until the viscous mechanism of Miles (1962*a*) takes over. Then waves and air flow become coupled; the waves give rise to a pressure distribution at the water surface which feeds energy to the waves at a rate which increases with the amplitudes of the waves. Unless viscous dissipation exceeds the energy gain due to the induced pressure, single components of the wave spectrum grow exponentially with time or with fetch under the action of a steady wind.

The Phillips–Miles mechanism is appealing because it promises a rational solution to an age-old problem, but it seems that the part of the theory that deals with the initiation of waves is at odds with observation that the first waves form a regular pattern. If turbulence were responsible for these first waves, one would expect their pattern to be fully random. There is also some evidence that the quantitative results based on the theory are not in agreement with experiments. A preliminary attempt to verify the Phillips–Miles theory by Hidy & Plate (1966) failed to reveal a régime of linear growth in the development of a wave component with fetch or time. All frequency components examined in that study grew approximately exponentially. However, it was found that the growth rate was not equal to that predicted by Miles (1962*a*), but was about twice too large. There was some scatter in the experimental data, but the trend towards larger growth rates than predicted analytically was quite definite.

These results of Hidy & Plate (1966) cannot be considered conclusive because not all conditions required by the theory were met in the experiments. For example, the shearing stress acting on the water varied with fetch, and a drift current developed in the water. Both of these features were not taken into account in Miles's model. We therefore felt that more accurate experiments were needed to clarify features of the mechanism of wave generation by wind. The results of such tests are reported in this paper.

The experiments were of two different types. The first series was directed towards a better understanding of the interaction of the turbulent wind field and the first waves. We observed the development of the waves from their inception, when the water surface is virtually glassy smooth, to fully developed waves, for two different air speeds. The variation in the water surface elevation was determined with a newly designed capacitance gauge capable of detecting water surface undulations of less than ten microns in amplitude. For similar conditions, single wire hot-wire anemometer measurements were made in the air flow, from which turbulent intensities and spectra were determined. No evidence of the effect of waves could be found in the turbulence, nor could a significant difference between turbulence over a smooth plate and a smooth water surface be detected. Additional experiments on the role of the turbulence showed

that an increase in the intensity of the turbulence outside of the boundary layer leads to a lowering of the critical water surface shearing stress, and that the turbulence propagates at a much faster speed over the surface than the speed of the water surface waves. We conclude that turbulence is probably not directly responsible for the first observable waves.

The second experiment was designed to duplicate as closely as possible the conditions for the validity of Miles' model. The shear stress over the water surface was found to be constant at low wind speeds, up to fetches well beyond the appearance of the first waves. Also, the mean wind velocity distribution was closely logarithmic. The only feature not provided for in Miles' model is the

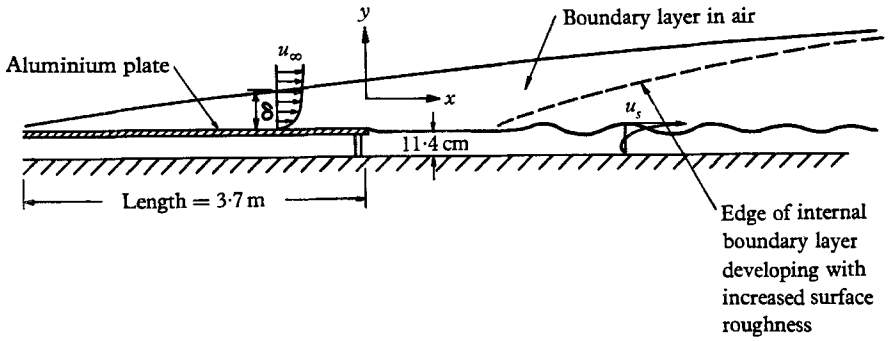

FIGURE 1. Schematic diagram of the experimental arrangement of combined air and water flow.

drift current in the water. To check for its possible influence, the model of Drake (1967) is utilized to calculate growth rates. This model in which the drift current is considered as additional variable is a modification of Miles' model. It yielded growth waves which were in slightly better agreement with experiments than Miles' model.

2. Experimental equipment and procedures

The experiments were performed in a wind–water tunnel which has been described in detail by Plate (1965). The experimental arrangement is shown in figure 1. Air flows from the tunnel inlet over a smooth flat plate of 3·7 m length on to a body of initially standing water, 11·4 cm deep and 13·7 m long. The fetch x is measured positive downstream from the junction between the plate and the water. The flat plate consists of smoothly sanded aluminium. Screens and a honeycomb section placed at the tunnel inlet assure an aerodynamically smooth flow developing over the bottom which corresponds to flow in a developing turbulent boundary layer.

Measurements taken in this study include records of the water surface displacement, profiles of mean air velocity, turbulent fluctuations of the longitudinal component of the air flow, apparent critical wind speeds, and velocities of the drift current at the water surface. To measure the water surface displacement, a

capacitance gauge was used which consisted of a 32-gauge, Nyclad-insulated magnet wire combined with a bridge circuit developed in the Engineering Research Center of Colorado State University. This capacitance device had a sensitivity which permitted the measurement of water surface undulations with amplitudes of less than ten microns. For such low amplitudes, even a wire as thin as the one employed here is not free of capillary adhesion effects. Consequently, the data should be accepted with reservation at lowest wind speeds until verified by other investigations. At the high wind speeds, however, the wave heights were significantly larger than ripples found in lower wind speeds even at the shortest fetches, so that the results can be used with confidence.

The capacitance probe was practically free of drift in the bridge circuitry. A tendency for drift was observed only at the very highest sensitivities, and over much longer times than any sampling time used.

The data of wave amplitude were recorded on a Brush Mark III strip chart recorder (with a frequency response curve flat to 30 Hz) and were digitized manually for computer analysis. Usually, points were taken at time intervals $\Delta t \simeq 0{\cdot}025$ sec, for a total of about 2000 points. Calculations of the statistical properties of the wave records included the standard deviation σ, the autocorrelation function $R(\tau)$, and the energy spectral density $\phi(n)$. The maximum lag $\tau_{\max}$ was chosen at $\tau_{\max} = 200\Delta t$, yielding $k = 2n\Delta t/\tau_{\max} = 20$ degrees of freedom. For such computations, techniques were used which have been described previously by Hidy & Plate (1966).

Mean velocity measurements in air were made by continuously recording on an x–y recorder the dynamic pressure of a Pitot-static tube versus signal proportional to the distance from the undisturbed water surface as the probe moved vertically through the air stream. Turbulent fluctuations were measured with a Hubbard-type hot-wire anemometer, working on the constant temperature principle. The probe containing the hot wire was held stationary at a given position for 5 min. While the root-mean-square (r.m.s.) value of the signal was read, the turbulence signal was recorded on an FM tape recorder. The r.m.s.-meter used measured 99 % of the fluctuating signal above 2 Hz. The spectra of these records were determined with a Bruel and Kjaer analogue spectrum analyzer (type 2109), with proportional one-third octave filters. The low-frequency range of the spectrum was investigated more closely with a spectrum analyzer made by Technical Products (type TP 627) which has constant bandwidth filters of 2 Hz with a continuously variable centre frequency.

It was found that a critical wind speed could be defined at a given fetch as the speed of the air at a fixed reference location at which the vibrations of the water surface became visible. During such a test, the water surface was observed by watching the reflexions of the capacitance wire in it, as indicated in figure 2, plate 1. At wind speeds below critical the reflexion was a straight line which, with increasing wind speed, first oscillated irregularly in time with ever-increasing amplitude and then disrupted. The critical wind speed to which frequent reference will be made hereafter was defined rather arbitrarily as the speed at which, at a given fetch, the reflexion was still sinusoidal but on the verge of transition to the disrupted stage as shown in figure 2 (*b*).

Velocities of the drift current at the water surface were measured by observing the motion of paper disks of 0·6 cm diameter cut from thin wax paper, and timing the passage of the paper particles between distance markers. The distance markers consisted of strips of adhesive tape glued to both transparent walls of the wind–water tunnel, across which the disks' passage was sighted. At the time of passage, a switch was thrown which would apply a voltage to a voltage–time recorder. At the passage of the next strip, the switch was thrown again, and a downward step was obtained. In this manner, a single particle could be timed at all marks along the channel. Twenty particles were traced and averaged for the determination of each case of water surface speed.

3. Results

3.1. *Air motion over very small waves*

Experimental conditions were restricted primarily to cases where the shearing stress at the water surface was constant with fetch and time and the disturbances on the water surface were as small as possible yet still observable. Under these circumstances, the surface stress was uninfluenced by the induced surface roughness, so that all analytical models should apply which assume no coupling or weak coupling between the air and water motion. For completeness, however, and for comparison with previous work, a few measurements of air flow and water surface agitation are cited in a range where the surface stress increased downstream with the influence of the growing waves. We begin by presenting typical aerodynamic data to show that the water did not affect the air flow in the régimes of principal interest in so far as we were able to determine with our experimental equipment.

Mean velocity profiles. Two different régimes of air flow were examined in this study, one at low wind speed in the 'critical' régime of $u_\infty \approx 3$ m sec^{-1}, and one at higher wind speed of $u_\infty \approx 11$ m sec^{-1}. Here u_∞ refers to the speed of the air stream outside the boundary layer, whose thickness δ is defined as the height at which the mean wind speed $\bar{u}$ is equal to 0·99 u_∞. All of the measured wind profiles are well correlated by a logarithmic form:

$$\frac{\bar{u}(y)}{u_*} = \frac{1}{\kappa} \ln y/z_0, \tag{1}$$

where u_* is the square root of the ratio of the stress at the water surface τ_0 to the air density ρ_a. Kármán's constant, κ, is taken as 0·40, and z_0 denotes the roughness length. Typical parameters for the mean air flow are listed in table 1.

In the low-speed cases, waves could be identified visually only downstream of the critical fetch, while, at the higher wind speeds, waves appeared immediately after the edge of the aluminium plate. At all wind speeds, the distributions of average longitudinal velocity were found to follow the logarithmic law, (1), in the lower portion of flow. At distances far downstream in the high-speed flow, departures from the logarithmic profile were observed, but this régime will not concern us here. In cases where the wind profiles were logarithmic, u_* was estimated from the slope of the lower portion of the profile. Because of the rapid

x (cm)	u_∞ (m sec^{-1})	u_* (cm sec^{-1})	δ (cm)	z_0 (cm)	Remarks
488	3·66	15·8	7·62	$9{\cdot}6 \times 10^{-4}$	Critical fetch without grid
488	3·20	13·4	5·72	$11{\cdot}2 \times 10^{-4}$	Critical fetch, with grid
−35·3	10·6	45	4·8	$3{\cdot}3 \times 10^{-4}$	Over plate
244	11·1	62·4	6·8	$8{\cdot}02 \times 10^{-3}$	Over initial ripples ($\sigma \approx 0{\cdot}3$ cm)
850	12·8	82·5	15·0	$3{\cdot}82 \times 10^{-2}$	Over fully developed waves ($\sigma \approx 0{\cdot}9$ cm)

Table 1. Typical characteristics of the mean flow of air.

growth of waves at the higher wind speeds, u_* remained constant under these conditions only for a fetch $x \leqslant 50$ cm. These results have been discussed previously for slightly different conditions of air flow by Plate & Hidy (1967).

Equation (1) is often written in the form of the law of the wall

$$\frac{\overline{u}(y)}{u_*} = \frac{1}{0{\cdot}40} \ln \frac{u_* y}{\nu_a} + \text{const.}, \tag{2}$$

where ν_a is the kinematic viscosity of the air, and the constant is related to the roughness length, z_0. Typical mean velocity profiles in the air are shown in this form in figure 3. The constant in (2) found for flow over the aluminium plate is 5·6, which is somewhat larger than the value of 4·9 quoted by Clauser (1956) but it has been observed by many workers that this constant can vary over a range between 4·3 and 6. The two profiles shown for larger fetches agree with (2) except for the numerical constant, which is found to be negative. This is typical for flow over fully rough boundaries. Corresponding values of z_0 are given in table 1.

For wind profiles taken at low speed over water, the constant in (2) was found to be equal to 6·1. The agreement with the results for flow over smooth solid boundaries could be improved by correcting the air velocity profiles for the effect of the drift current. Taking the air flow relative to the velocity u_s of the drift current at the surface, i.e. substituting $\overline{u} - u_s$ for $\overline{u}$ in (2), one obtains close agreement with the value of 5·6 by using $u_s/u_* = 0{\cdot}57$ obtained from observations of surface drift at this wind speed.

The two distributions taken at low speeds in figure 3 correspond to the critical wind speeds at fetch $x = 488$ cm. One set of data was obtained with a flow developing with usual inlet conditions. The second set of data was taken under inlet conditions modified for creating a high turbulence level in the air flow. The turbulence was increased by placing a heavy grid of 2·54 cm wide slats nailed crosswise at distances of 5·08 cm at the upstream edge of the aluminium plate. These two conditions correspond to different boundary-layer thicknesses, and different velocities in the free stream as well as different shearing velocities

(table 1). The reason for changing the air turbulence level will be discussed in a later section.

Turbulence properties. Turbulence measurements were restricted to determination of the fluctuations u' in the longitudinal component of the air velocity. The variance of the turbulent fluctuations, $\overline{u'^2}$, was measured as a function of height from the mean water level for the high ambient air speed over several different fetches. These results are shown in non-dimensional form in figure 4(*a*). The quantity $(\overline{u'^2})^{\frac{1}{2}}$ has been normalized by u_* and plotted with y/δ. The data taken at high wind speeds over the plate are compared with results of Klebanoff (1954)

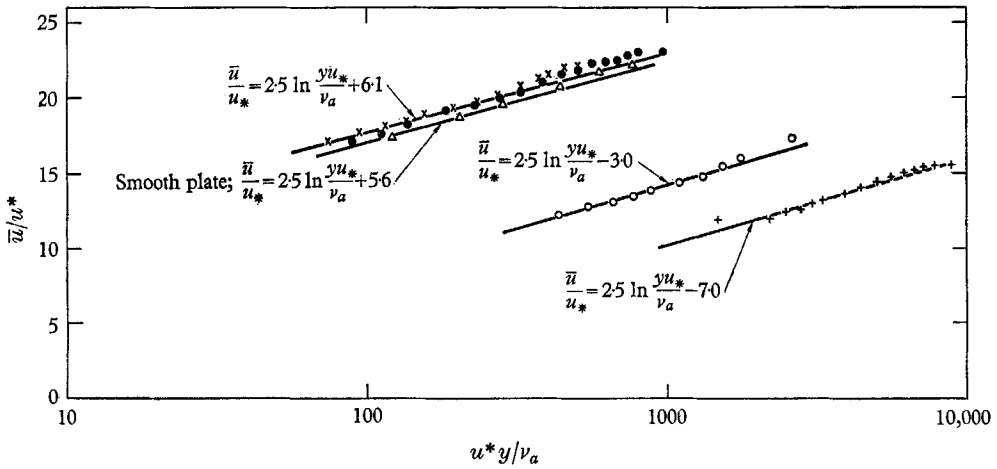

FIGURE 3. Distribution of average air velocity in the downstream direction at various fetches, with and without inlet grid. ●, u_* = 15·8 cm/sec without grid, x = 488 cm; ×, u_* = 13·4 cm/sec with grid; △, u_* = 45 cm/sec (smooth flat plate), x = −35·3 cm; ○, u_* = 62·4 cm/sec, x = 244 cm; +, u_* = 82·5 cm/sec, x = 850 cm.

and satisfactory agreement is found, except in the outer portion of the boundary layer where the higher free-stream turbulence caused deviations. Over the waves the $\overline{u'^2}$ profiles are similar in shape to that of the profiles of Klebanoff (1954), but the dimensionless quantities $\overline{u'^2}/u^2$ are somewhat larger for a given thickness δ. Evidently, the turbulence in the developing boundary layer over the waves is not in equilibrium, in contrast to that found in fully developed boundary layers over uniform surfaces.

In comparing the observations of air turbulence taken at critical fetch, the boundary-layer thickness is not a meaningful scaling parameter because the change in the free-stream turbulence significantly distorts the outer part of the boundary layer, leading to a thickness which is much smaller for high free-stream turbulence. Since the two cases correspond to flow over smooth boundaries in the inner layer and differ in shear velocity only by 15 %, the profiles of intensity should be approximately similar in the lower boundary layer if plotted in dimensionless form based on the similarity parameters of the mean flow as given by figure 3. In figure 4(*b*), curves for $(\overline{u'^2})^{\frac{1}{2}}/u_*$ *vs.* yu_*/ν_a are drawn, showing striking agreement between the two cases near the boundary. In the outer part

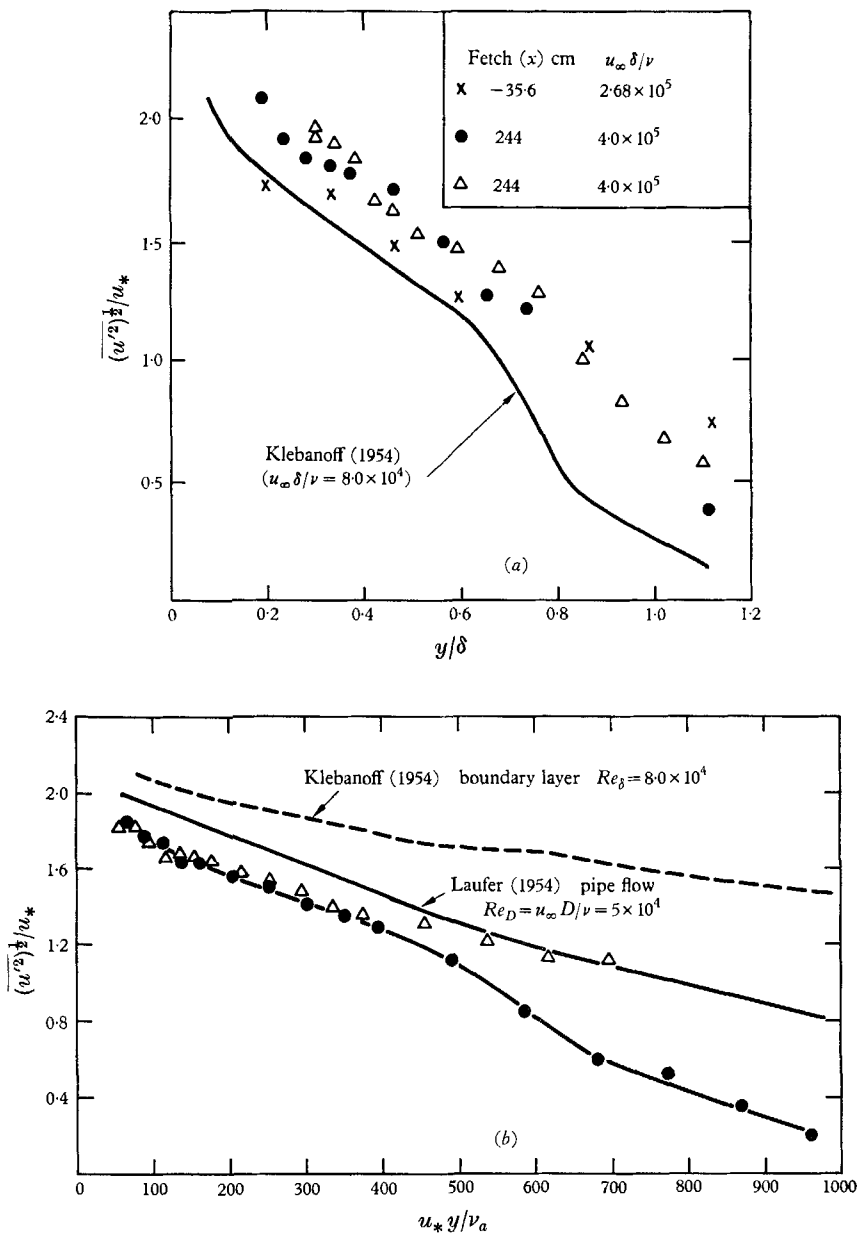

FIGURE 4. Distribution of intensities in longitudinal component of the air flow: (*a*) for $u_* = 45$ cm sec^{-1} at different fetches; (*b*) at $x = 488$ cm: ●, $u_* = 15{\cdot}8$ cm sec^{-1} (without grid), $Re_\delta = 1{\cdot}9\times10^4$; △, $u_* = 13{\cdot}4$ cm sec^{-1} (with grid), $Re_\delta = 1{\cdot}1\times10^4$. Curves of Laufer (1954) and Klebanoff (1954) are added for comparison. Laufer's results correspond to fully developed pipe flow with Reynolds number based on pipe diameter D.

of the boundary layer the grid turbulence, of course, influences the intensity profile strongly. However, the curves in figure 4 (*b*) do not agree with smooth plate data of Klebanoff (1954). There seems to exist a systematic variation with Reynolds number, as suggested by comparison between Laufer's (1954) data for pipe flow, and Klebanoff's (1954) results in a wind tunnel.

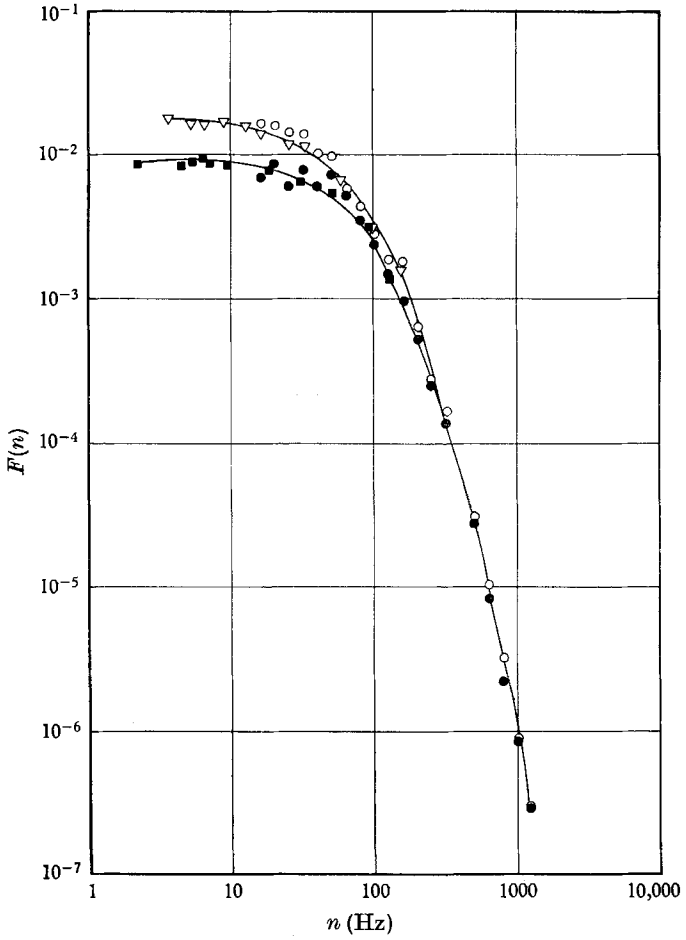

FIGURE 5. Spectra of air turbulence at critical fetch of $x = 350$ cm, $y = 1{\cdot}27$ cm with $u_* = 17$ cm sec^{-1} (without grid), and $u_* = 15{\cdot}8$ cm sec^{-1} (with grid). ○, without grid, proportional band-width analyzer; ▽, without grid, constant band-width analyzer; ●, with grid, proportional band-width analyzer; ■, with grid, constant band-width analyzer.

From analysis of magnetic tape recordings of the signal from the hot-wire anemometer, energy spectra for the longitudinal velocity component of air flow were determined. Some typical examples plotted in frequency co-ordinates are shown in figure 5. These spectra represent data taken at critical wind speeds at a fetch of $x = 350$ cm, for $u_* = 17$ cm sec^{-1} ($u_\infty = 4{\cdot}0$ m sec^{-1}). They display a distribution of turbulent energy with frequency that is characteristic of known turbulent flows (e.g. Hinze 1959).

The modification of the energy distribution caused by changing inlet conditions is readily seen in the examples of figure 5. At small elevations above the water surface, say $y = 1{\cdot}27$ cm, the spectra were influenced by the presence of the grid mainly at low frequencies. The relatively high level of turbulence induced by the grid in the outer portions of the boundary layer tended to be associated with the large eddies, while at higher frequencies the energy distribution is nearly the same with or without grid. Consistently with the well-known concept of persistence of large eddies, the energy density associated with the low-frequency régime of the case with inlet grid does not change much with height. The variation in energy distribution with height is mainly the result of decreases with elevation in energy density in the smaller scale motion. It is interesting that, in the case with the inlet grid, the higher level of turbulence in the free stream was accompanied by much smaller decrease with height in energy over all frequencies in contrast to other cases.

Apparent rates of energy dissipation were calculated based on the assumption of isotropy in the small scales of turbulent motion. For this assumption, the dissipation rate ϵ per unit mass becomes (Hinze 1959):

$$\epsilon \approx 15\nu_a \overline{\left(\frac{\partial u'}{\partial t}\right)^2} \frac{1}{\overline{u}^2}. \tag{3}$$

We have evaluated $\overline{(\partial u'/\partial t)^2}$ from the one-dimensional energy spectrum through the relation

$$\overline{\left(\frac{\partial u'}{\partial t}\right)^2} = (2\pi)^2 \overline{u'^2} \int_0^\infty n^2 F(n)\, dn. \tag{4}$$

Here n is the frequency in Hz, and $F(n)$ in sec is the spectral density of turbulent energy associated with u', and divided by $\rho\overline{u'^2}$, in the frequency domain.

The spectral technique for calculating dissipation rates has also been employed by Pond, Stewart & Burling (1963) for turbulent winds over ocean waves. Since it is of interest to compare our data with theirs, the dissipation rates have to be defined on the same basis. However, the validity of the assumption of local isotropy in turbulent shearing layers is open to question. Klebanoff (1954), for example, has found that direct evaluation of dissipation rates in the boundary layer along a flat plate near the wall yielded about twice the rates estimated on the basis of the assumption of isotropy. Typical values of dissipation rates calculated from (3) and (4) are listed in table 2 along with values of the microscale λ_g calculated from

$$\lambda_g^{-2} = \left(\frac{2\pi}{\overline{u}}\right)^2 \int_0^\infty n^2 F(n)\, dn. \tag{5}$$

Distributions of ϵ as function of height and fetch for the case of high wind speed are shown in figure 6. Here data of Hess (1968) are also given for comparison. Both sets of data are seen to be in agreement. A strong increase in the apparent dissipation rate with fetch is observed in these results. The dissipation rate increases faster than production. If, as a first approximation, production is set equal to dissipation rate then one should obtain in the constant stress layer with $\overline{u'v'} \approx u_*^2$ that $\epsilon\kappa y/u_*^3 \approx 1$, where v' is the fluctuation of the vertical component of velocity.

x (cm)	y (cm)	u_* (cm sec^{-1})	$(\overline{u'^2})^{\frac{1}{2}}$ (cm sec^{-1})	$\epsilon \times 10^{-4}$ (cm^2 sec^{-3})	λ_g (cm)	$\epsilon\kappa y/u_*^3$
350	1·27	17	11	1·20	0·43	
(without	2·54		7·9	0·75	0·54	
grid)	7·62		2·6	0·16	0·66	
	12·7		1·0	0·07	0·66	
350	1·27	15·8	7·0	1·42	0·37	
(with grid)	2·54		4·0	0·42	0·51	
	7·62		1·5	0·20	0·58	
−35·3	0·51	45	114	17·0	0·48	0·38
(δ = 4·8 cm)	1·14		75	4·6	0·58	0·23
	2·42		56	1·8	0·71	0·19
	3·69		33	0·76	0·64	0·12
	6·22		10·2	0·033	0·94	0·09
244	1·27	62·4	127	16·8	0·51	0·36
($\sigma \approx$ 0·3 cm)	1·91		118	14·4	0·52	0·45
	2·54		111	11·1	0·55	0·46
	3·82		92	5·5	0·66	0·34
	5·08		75	3·0	0·73	0·24
850	4·42	82·4	161	29·8	0·48	0·98
($\sigma \approx$ 0·9 cm)	5·69		150	25·0	0·50	1·01
	6·96		134	16·5	0·55	0·81
	8·86		120	11·0	0·60	0·69
	14·0		69	2·7	0·70	0·29

TABLE 2. Turbulence characteristics of the air motion.

If this number is larger than 1, then dissipation exceeds production. If it is smaller than 1, production exceeds dissipation and the turbulent intensity increases with distance. Calculated values of $\epsilon\kappa y/u_*^3$ are listed in table 2. Although the dissipation rate increases with fetch more rapidly than the production, the absolute magnitude of production is found to be larger at all fetches, except for the largest, where balance of dissipation and production is found near the surface.

The turbulent energy spectra calculated for flow over the waves could be represented non-dimensionally over most of the high wave-number ranges by a similarity profile. The scaling parameters were those required by Kolmogoroff's $-\frac{5}{3}$ law for the inertial subrange. The dimensionless spectrum is given by

$$\psi(k/k_s) = BF(n), \tag{6}$$

where

$$B = \frac{\overline{uu'^2}}{2\pi}(\epsilon\nu_a^5)^{-\frac{1}{4}}, \tag{7}$$

$k = 2\pi n/\bar{u}$ is the wave-number and $k_s = (\epsilon\nu_a^{-3})^{\frac{1}{4}}$ is the reference wave-number. Spectra for several fetches are recalculated in this framework using ϵ from (3) and are shown in figure 7.

All spectra shown have a well-defined viscous dissipation range at the high wave-numbers. In this range, the spectra fall on the same curve, which agrees

with the universal form found, for example, in thicker turbulent layers by Sandborn & Marshall (1965). Adjacent to the low wave-number extreme of the dissipation range, there may exist an inertial subrange. Pond *et al.* (1963) found that for spectra over ocean waves the $k^{-\frac{5}{3}}$ decrease holds over many decades of wavenumbers. Their average curve has been plotted with the experimental spectra of figure 7. With the exception of spectra corresponding to very thick boundary

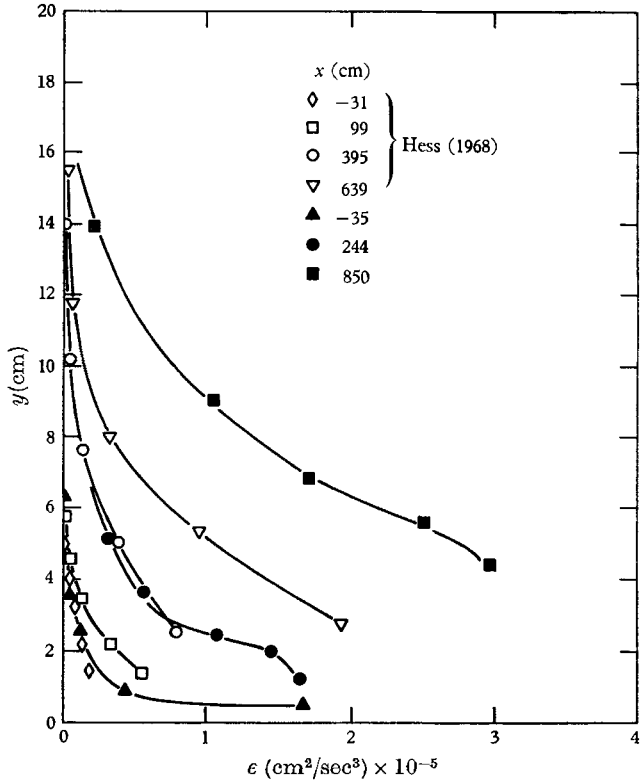

FIGURE 6. Distribution with height of the apparent rate of dissipation for air flow over small waves.

layers, such as those measured by Sandborn & Marshall (1965), laboratory boundary layers do not usually show a well-defined $-\frac{5}{3}$ power law. This is also found over waves when the free-stream turbulence level is low. However, for grid-induced high free-stream turbulence levels, the spectra contain a small inertial subrange, which furthermore agrees with that of Pond *et al.* (1963). This is illustrated in figure 7(*c*), where the spectra corresponding to critical wind speed at a fetch $x = 3{\cdot}50$ m with grid turbulence are reproduced.

For the conditions of low free-stream velocity, or for conditions near the outer zone of the air flow responding to changing surface roughness, the Kolmogoroff constant K, as defined by

$$\psi(k/k_s) = K(k/k_s)^{-\frac{5}{3}}, \tag{8}$$

deviates from the value of 0·46 reported by Pond *et al.* The value of 0·46 probably corresponds to a turbulent medium which is in local equilibrium when the dissipation rate ϵ equals the production rate.

3.2. *Wind-induced water motion*

The measurements of the turbulent shearing flow in air over the water characterize the conditions for energy transfer to the water. Under the influence of the air motion, waves are raised, and a drift current develops.

The wind waves. As the steady wind is gradually increased in speed from zero, the water surface at any given point undergoes gradual changes from glassy smooth to fully developed waves. This is illustrated by the sequence of photo-

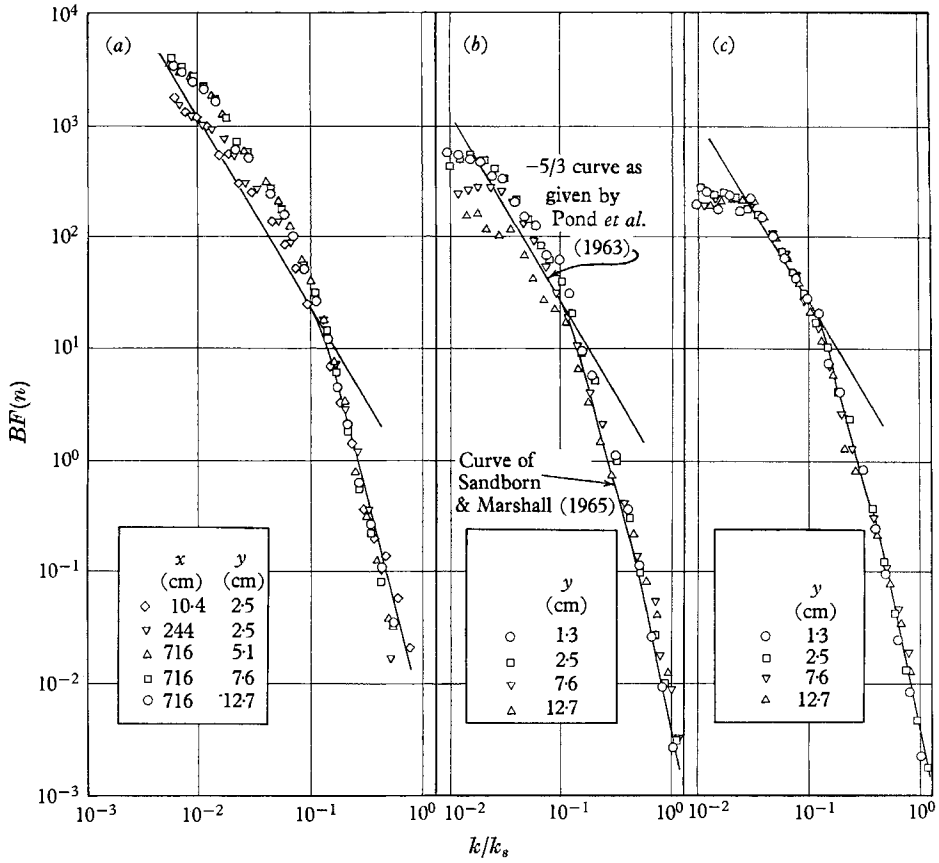

FIGURE 7. Non-dimensional spectra of turbulence in longitudinal component of air flow. (*a*) $u_* = 45$ cm sec^{-1} for typical heights and fetches. (*b*) $u_* = 17$ cm sec^{-1} (without grid) at $x = 350$ cm. (*c*) $u_* = 15{\cdot}8$ cm sec^{-1} (with grid), $x = 350$ cm.

graphs shown in figure 8, plate 2. The first waves, near critical wind speeds, are smooth undulations, two-dimensional in appearance, which are oriented with crests nearly perpendicular to the direction of flow (figure 8 (*a*) and (*b*)). As the wind speed increases, the water surface becomes somewhat more ruffled (figure 8 (*c*), (*e*) and (*f*)). Short crested capillary ripples are superimposed over the first undulations (figure 8 (*c*) and (*e*)) and a rhombic wave pattern develops. With further increase in velocity the rhombic pattern evident in figure 8 (*c*), (*e*) and (*f*) re-orders

itself into a more two-dimensional wave pattern where the waves are slightly skewed with longer and smoother backs than fronts (figure 8 (*d*), (*g*) and (*h*)). The capillary ripples which were originally distributed rather uniformly over the surface become concentrated on the wave-fronts and align to form more or less

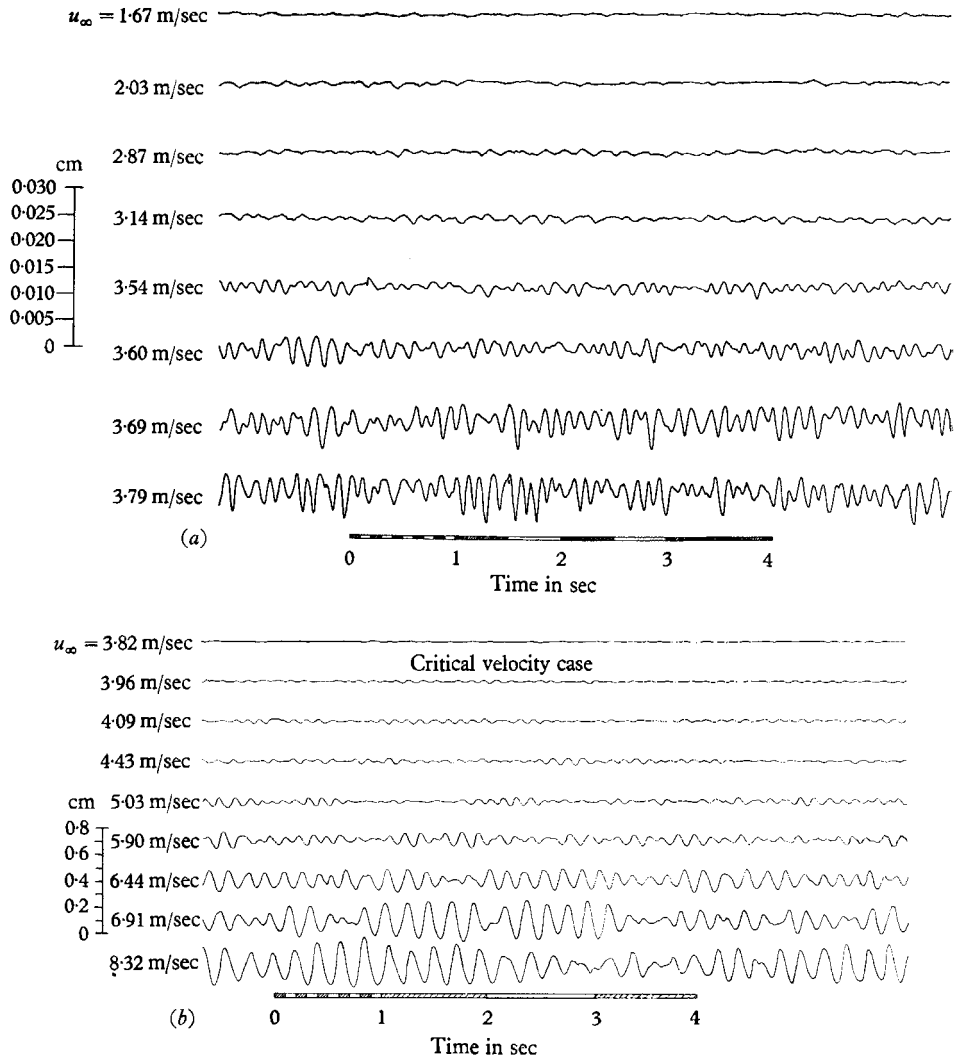

FIGURE 10. Typical recordings of capacitance gauge response near critical wind speed (with grid). Data shown are for different wind speeds at x = 3·50 metres. (*a*) Records taken at high sensitivity of the wave gauge below critical wind speed. (*b*) Records similar to those in (*a*), but taken at much lower sensitivity, wind speed higher than critical.

uninterrupted ridges in front of the wave crest. They have a maximum amplitude near the crest of the wave, on which they are superimposed, and diminish in size towards the valley of the large wave, where they disappear altogether. The ripples have a wavelength which lies between 0·5 and 1 cm, and they appear to stay with the larger wave on whose front they ride. The general appearance of the

water surface is then as shown in figure 8 (*f*) and (*h*). In figure 8 (*f*), the ordering process of the ripples has just begun, and in figure 8 (*h*) it is essentially completed. The pattern is thus seen to be similar to the development described qualitatively by Phillips (1966).

If the wind speed u_∞ is increased beyond 10 m sec^{-1} the early evolution of ripples pictured in figure 8 (*a*), (*b*) and (*h*) is not so easily observed. Instead, it is compressed into a short distance very near the inlet plate. This can be seen in figure 9, plate 3. At longer fetches and high wind speeds, the capillary ripples are observed to emerge both on the windward and leeward sides of the two-dimensional, dominant waves, as observed earlier by Hidy & Plate (1966).

The records of water surface displacement taken at one point under conditions similar to those for the photographs in figure 8 are shown in figure 10. They were taken at $x = 3{\cdot}5$ m for different wind speeds around the critical value. They give further information about the nature of the onset of visible waves on the water surface. Two striking features are revealed in the traces of figure 10. First, the recordings show quite clearly that microscopic undulations exist at velocities well below the critical wind speed even though they are not readily visible. Even at the lowest wind velocities occasional bursts of tiny wavelets were observed whose amplitudes exceeded the sensitivity threshold of the capacitance gauge at practically all wind velocities. However, in order to become clearly visible, they must have been exposed to the wind for some time; that is, they must have travelled downwind. They become recognizable at wind speeds slightly below critical. At critical conditions, these first undulations appear visually to be on the verge of breaking up into the rhombic pattern.

Secondly, it is observed that the process of wave growth takes place in the following manner. At the lowest wind speeds, the apparently calm surface is occasionally interrupted by the passage of a small group of waves which are just of sufficient height to penetrate the sensitivity threshold of the capacitance gauge. With increase in wind speed, the wave groups accumulate more waves, but grow only very little in amplitude until the groups join and form irregular interference patterns near their joints. Further increase in wind velocity leads to a growth in amplitude of individual waves which is again followed by adjustment in height of the adjacent waves. This process appears to repeat itself with increasing wind speeds, so that it is always possible to distinguish well-separated groups of waves, displaced with respect to each other by random phase shifts, but well defined and quite regular in themselves.

In addition to the records in figure 10, a series of wave-gauge traces were taken upstream and downstream of the 'critical fetch' at constant wind speed. A typical set of spectra $\phi(n)$, where $\phi(n)$ is the density of the potential energy of the Fourier component associated with frequency n, calculated from such data is drawn in figure 11. At fetches smaller than critical, the wave spectra are diffuse in the low-frequency range, falling off at high frequencies. The broadness of the spectra in this range may be an indication of the noise level and averaging or sampling error inherent in the digital analysis rather than of the presence of many Fourier components of nearly equal energy in the agitated surface. Just beyond the critical fetch, the spectrum begins to sharpen up as energy is transferred at

a maximum rate to a narrow band of waves whose frequency is centred around 8·5 Hz. With increasing fetch, the spectrum remains nearly constant in shape and has its maximum at 8·5 Hz until the peak reaches a curve which denotes an equilibrium limit. The equilibrium range is a curve denoted by (Phillips 1966)

$$\phi(n) = \beta g^2 n^{-5}, \tag{9}$$

where g is the acceleration of gravity, n is given in Hz, and β is the constant of proportionality, approximately equal to $7{\cdot}5 \times 10^{-6}$. This equilibrium range has been found to exist for waves varying from those observed on laboratory scales to ocean waves (Hess 1968). Growth of frequency components far beyond the equilibrium limit denoted by (9) does not appear possible. Instead, a continued increase in energy of a wave train at this stage tends to be associated with a shift of the spectral peak to lower and lower frequencies.

There may be a significance in (9) which goes beyond the intention of Phillips to describe the high-frequency end of the spectrum. In fact, the spectral curves do not really follow very well the dependency expressed by (9). Near the peak, the decrease in energy is much steeper, more like an n^{-9} drop-off until a secondary peak, at twice the frequency of the primary peak, is reached. At still higher frequencies, the drop-off continues at a higher rate than n^{-5}. This was also found by Sutherland (1967). A well-defined n^{-5} subrange cannot be found for the laboratory data except by drawing a somewhat arbitrary curve through all parts of the high-frequency end of the spectrum. However, if all spectra are considered together, then (9) is found to denote an average curve through the high-frequency ends of all spectra, which is overshot somewhat by the spectral peaks. By a small adjustment of the constant β it is possible to make (9) the envelope to the peaks of all spectra, rather than to the high-frequency end. In this form, (9) can be interpreted as a limit to the growth rate of all spectral peaks, quite independent of the high-frequency end of the spectra, or the spectral shape. In an appendix, we offer an alternative derivation of (9) which is based on the assumption that the peak corresponds to a dominant wave whose amplitude is limited by gravity.

While for peak spectral densities below equilibrium the frequency remains constant at constant shear velocities, it was observed that an increase in wind velocity has a tendency to shift the peak of the unsaturated wave spectrum to lower frequencies. In a set of experiments ranging from $u_* = 17$ cm/sec to $u_* = 35$ cm/sec the peak was seen to move from 7 to 11 Hz. The results are tabulated in table 3. The experiments also led to a decrease in fetch length at which critical wind speeds for wave appearance were observed.

An illustration of the spectra found under conditions of higher wind speeds is shown in figure 12. These data correspond to the evaluation of the agitated surface at $u_\infty \approx 10$ m sec^{-1}. Close to the plate at $x \leqslant 5$ cm, the spectra display a peak at $n = 16$ Hz which is attributed to the tunnel vibrations. The natural vibrations of the tunnel were examined and found to be nearly sinusoidal with a frequency of about 18 Hz, governed by the rotational speed of the fan, which was constant for all wind velocities. The 16 Hz peak is quite pronounced at $x = 1$ cm. By $x = 5$ cm, this component has become secondary in importance to a wind-induced component at a frequency of about 11 Hz. This shows that the dominant

wave is not associated with tunnel vibrations. At fetches up to 50 cm, the 11 Hz component is predominant in the spectra. In this case, therefore, it appears that this component represents the wave of maximum growth over a fetch of from 0 to 50 cm. For this fetch a constant shearing stress of $u_* = 35$ cm sec^{-1} was determined as previously reported by Plate & Hidy (1967). At a fetch of about 40 cm, the 11 Hz component reaches the equilibrium curve, and from then on the frequency associated with the dominant peak decreases with increase in fetch, as has been observed in the case of flow at low velocities.

u_* (cm sec^{-1})	Frequency of spectral peak n_{max} (Hz)	Predicted frequency of spectral peak based on Miles' theory with wave-number corrected for drift current (Hz)
15·8	7·0	9·2
16·2	7·0	—
17·0	7·5	9·2
19·0	8·5	9·3
19·8	9·0	—
35·0	11·0	12·8

TABLE 3. Increase in frequency of spectral peak with wind speed in the second stage of growth.

Series of spectra taken at increasing fetches such as those shown in figures 11 and 12 enable the tracing of the growth of a particular Fourier component. Two results of this kind are shown in figure 13, in which the development of the spectral peaks before saturation is illustrated. These curves indicate that the 11 Hz component of the high wind spectra follows an exponential growth law up to about 40 cm fetch where equilibrium is attained. The growth rates for the spectra taken for conditions of low wind speed generally were not nearly as well defined. The case for $u_* = 19$ cm sec^{-1}, in figure 13, displays a region upstream of the critical fetch, $x \approx 200$ cm, where the growth rate is small. However, from about $x = 100$ cm to conditions where equilibrium is attained for the 8·5 Hz component at $x \approx 300$ cm, the spectral density increase is best fitted by a straight line of slope 6·5 m^{-1}, suggesting an exponential growth up to the equilibrium limit.

The drift velocity at the water surface. The velocity u_s of the water surface was measured by means of the technique described earlier in § 2. Results are shown in figure 14 for two different friction velocities based on the air motion. It is observed that over short fetches the drift velocity increases roughly according to a power law, while, at fetches exceeding about 1 m, the ratio of the drift velocity to the free-stream velocity, u_s/u_∞, attains a constant ratio of 0·026. If a cross-sectional average wind speed is defined as $0{\cdot}8u_\infty$, these results agree with data obtained by Keulegan (1951) for large Reynolds numbers based on fetch.

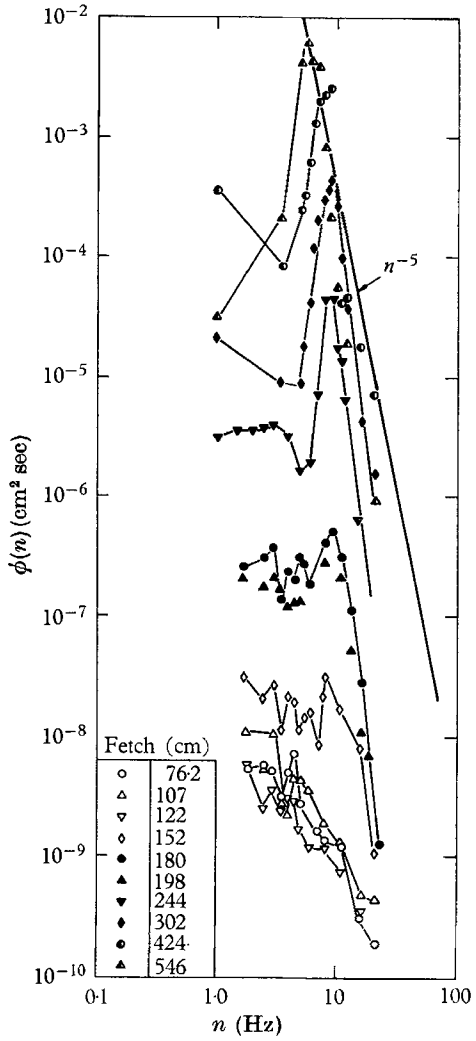

FIGURE 11

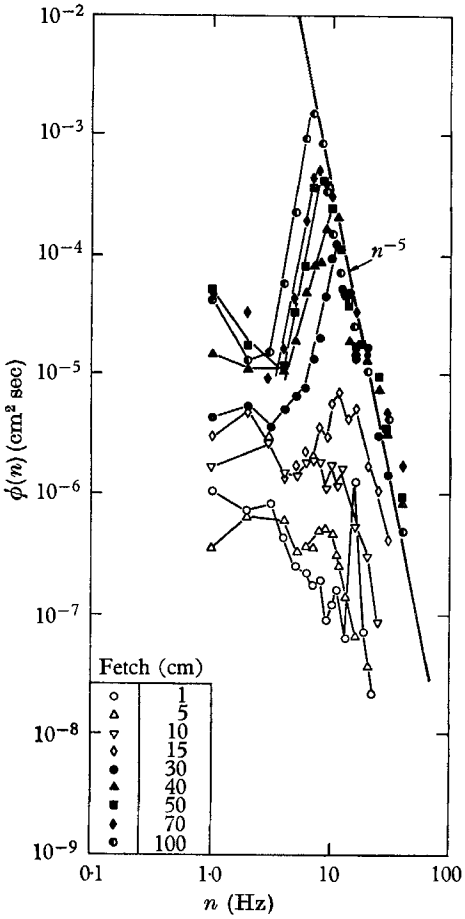

FIGURE 12

FIGURE 11. Amplitude spectra for wavelets being generated at low wind speeds. These records indicate the evolution of the spectra with fetch for $u_* = 19$ cm sec^{-1}.

FIGURE 12. Amplitude spectra for the waves developing downstream of the plate. $u_* = 35$ cm sec^{-1}.

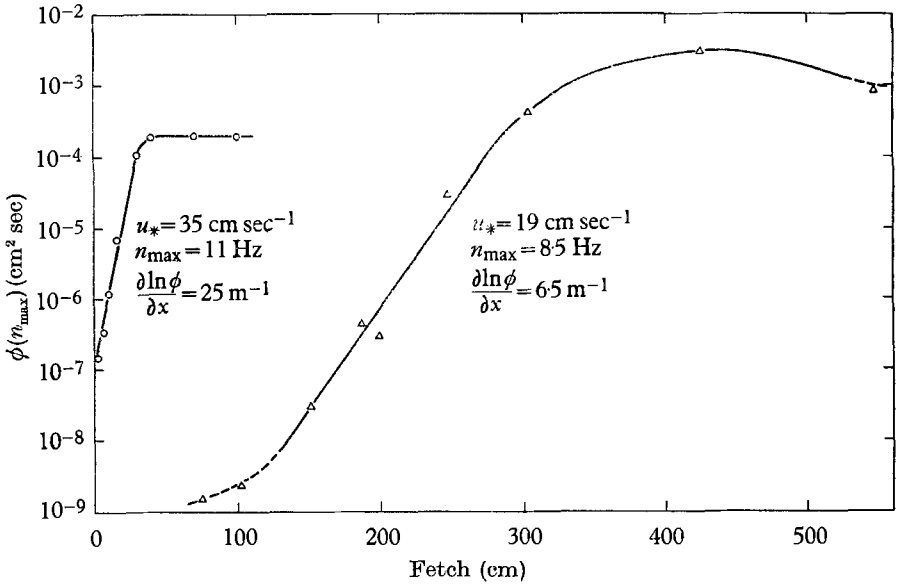

FIGURE 13. Growth with fetch of single components of the wave spectrum for $u_* = 35$ cm sec^{-1}, and $u_* = 19$ cm sec^{-1}. Wave components shown are for the spectral peak, whose frequency is n_{max}.

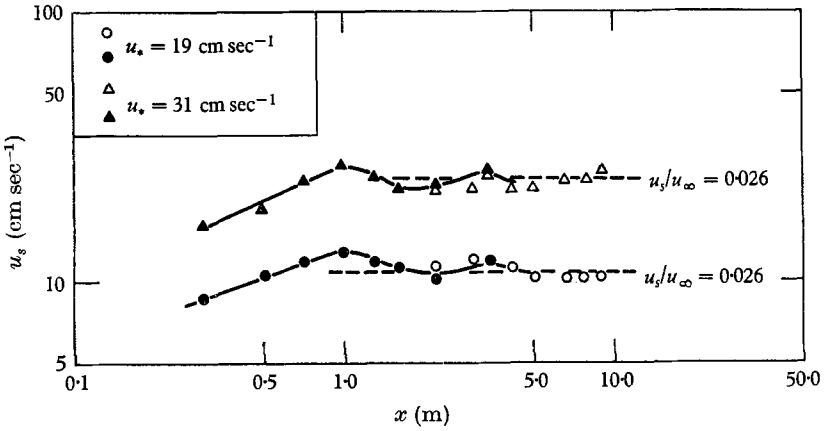

FIGURE 14. Typical distributions with fetch of drift velocity of the water surface.

4. Discussion

When air flows from a smooth solid surface on to water, the turbulent boundary layer evolves in essentially the same manner as it would have over a solid boundary. As long as the surface standard deviations do not exceed $\sigma \simeq 0{\cdot}10$ cm, the structure of turbulence remains characteristic of shearing layers over smooth boundaries (see also Plate & Hidy 1967). For waves of larger amplitude, the wind profile responds in its lower parts to the increasing roughness in a manner as expected for boundary layers along solid, rough surfaces. For our present data, examination of the mean flow, turbulent intensities and energy spectra of the longitudinal component, and apparent turbulent energy dissipation rates suggest no marked anomalies attributable to wave action on the air even over wavy surfaces whose standard deviation exceeds 0·1 cm, except possibly for the dissipation rates. Consequently, we conclude that the wind field is at most weakly affected by the water waves, and, since a region of constant shear with fetch can be realized, it should be possible to compare the data taken in the tunnel with predictions based on theoretical models such as Miles' (1962*a*). In the following sections we shall discuss the experimental results principally in the light of such theoretical concepts.

4.1. *Stages of development of the small waves*

The experimental observations showed that there are three distinguishable régimes in the evolution of surface waves. The first is a condition wherein essentially two-dimensional microscopic disturbances form on a nearly glassy surface. These tiny oscillations have a regular shape with crests oriented nearly normal to the wind direction, and with a well-defined frequency (figures 8 (*a*), (*c*) and 10), which depends on the magnitude of the shearing stress exerted on the water surface by the wind. This behaviour of the invisible waves is inferred from the appearance of the first visible waves. If the wave crests of the nearly microscopic disturbances were not oriented perpendicularly to the wind, a marked change in dominant frequency in the records of figure 10 would appear after waves became visible. In the latter case, the visible dominant waves were quite distinctively oriented with crests normal to the wind direction as shown in figure 8 (*a*) and (*b*). The regularity in appearance of the first waves at frequencies lower than 13 Hz suggests that the resonance mechanism of Phillips (1957) may be relatively unimportant in setting up the initial disturbances. This conclusion is strengthened by the observation that in none of the data could a linear growth rate be unambiguously identified as predicted by Phillips' model. Other results of supplemental experiments discussed below also bear on this conclusion.

In the second régime of development, the wave pattern evolves spontaneously into a cross-hatched pattern of three-dimensional configuration (figure 8 (*c*) and (*e*)). This change in pattern, however, cannot be detected directly in wave traces taken at only one point, because the three-dimensional nature appears to be related to the occurrence of shorter, capillary waves which superimpose over the regular wave pattern which existed earlier. The appearance initially of two growth stages characterized by two-dimensional oscillations supplanted by more three-

dimensional wavelets also was recognized by Cohen & Hanratty (1965) for wind ripples on thin layers of liquid.

The third régime is associated visually with a return to a pattern of more or less two-dimensional gravity waves on which are superimposed small capillary ripples (figure 8 (*d*), (*g*) and (*h*)). This régime is characterized by amplitude spectra which coincide with a 'universal' equilibrium range in the high frequencies (figures 11 and 12). The third régime of wave development appears to be the one best studied in previous investigations, and it seems to be the one of principal significance in relation to ocean waves or lake waves.

Present theoretical knowledge seems to be able to explain qualitatively the broad aspects of wind action on a water surface in the first stages of growth after the onset of microscopic disturbances until the attainment of equilibrium, but the origins of the first two-dimensional ripples on a microscopic scale cannot be considered explained at present. In an attempt to obtain further insight into the nature of the onset of the first disturbances in the water, two supplemental experiments were performed.

4.2. *Experiments on the role of pressure fluctuations in wave initiation*

Two tests were performed on the effect of changes in the turbulence structure in the air on the process of wave generation. In the first, the turbulence level of the air was significantly changed (figure 4 (*b*) and table 2) by inserting a grid into the air flow a short distance upwind of the inlet plate. At the same time the ambient wind velocity with the grid was decreased to 3·2 m sec^{-1} as compared with $u_\infty = 3{\cdot}7$ m sec^{-1} for the same case without the grid, maintaining a critical fetch at 4·88 m, where waves first became visible in the sense of the criterion described in § 2. The mean velocity distributions and turbulence intensities from these tests were compared with equivalent results obtained for the same critical fetch but without grid.

The experimental data on the mean velocity distributions shown in figure 3 do not indicate any differences in shape of the velocity profile or any significant changes in the nature of the shearing flow. Rather the profiles correspond in both cases to that for flow over a smooth solid boundary. The observed change in shearing velocity u_*, or shear stress, τ_0, is however, significant. The shear stress for the case without grid is approximately 20 % larger than that for the case with grid. Yet the turbulent intensity profiles shown in figure 4 (*b*) coincide in the lower portions (the 'inner layer') for both cases if non-dimensionalized by means of scaling based on the shear velocity. Hence, within the inner layer, the turbulent intensity at a given elevation above the water surface is actually lower for the case with grid. The increase of the free-stream turbulence due to the grid is felt mainly in the outer part of the boundary layer, where the intensity was larger. A set of spectra of the turbulent energy for the same elevation above the water surface, shown in figure 5, indicates that the difference in the 'inner layer' between the two cases is found in the low-frequency end of the spectra. The high-frequency ends of the spectra are identical. At the low-frequency end of the spectrum where the energy associated with water waves should be found, the spectral energy of the case with grid is much lower.

The results of this experiment suggest that, for a given wind speed, a higher turbulent intensity in the ambient air outside the boundary layer leads to an earlier triggering of the disturbances of the water surface. From this observation, one might conclude that an analogy with transition to turbulence in a boundary layer exists, which also can be triggered by increasing the level of the turbulent intensity in the free stream. In our experiments, however, the air flow is already turbulent even at the shortest fetches. Tollmien–Schlichting waves in the air must therefore be ruled out as initiators of the first water surface waves. Thus, if the initial waves are a result of a transition from laminar to turbulent motion, it can only be a transition in the water. In the first metre or so the flow in the water appears to be laminar in nature, but farther downstream a transition to turbulent flow takes place. This was ascertained from observations of hydrogen bubble traces released in the water near the surface at conditions near critical wind speed at a fetch of 3·5 m. At low air velocities, the bubble pattern passed through a stage where small low-frequency oscillations apparently associated with secondary circulation are the only observed disturbances of the water current near the surface. With increasing wind speed occasional large eddies are shed from the thin layer of accelerated fluid near the surface into the interior of the water. At still higher wind speeds when the first waves become visible at the surface, the flow near the surface exhibits the eddying characteristics of fully turbulent motion. Thus, it appears that visible waves and turbulence in the water occur under identical conditions. An attractive speculation leads thus to a model of wind wave generation from perturbations induced by the air turbulence of the shear flow in the water. Against this stands the requirement that the disturbance for which the water boundary layer becomes unstable travels with a progression speed which is lower than the surface velocity, so that the critical layer at which the current velocity equals the phase speed of waves would be found in the water. This is contrary to observation which shows that all waves travel with phase speeds exceeding the water surface velocity.

An alternative interpretation of the experimental results might be given by postulating an initiation mechanism which produces comparatively well-ordered large-scale and low-frequency pressure oscillations associated with the air turbulence in the outer portion of the boundary layer. Such oscillations might develop a resonance with free modes of the water surface, equivalent to the mechanism of resonant interactions predicted by Phillips (1957).

To verify this latter model, pressure fluctuations should be measured at the surface. This is not possible with our present techniques. However, the pressure fluctuation pattern can be inferred from the pattern of the longitudinal velocity components $\overline{u'^2}$ by the following reasoning.

Willmarth & Wooldridge (1962) have shown a large degree of correlation between pressure fluctuations and fluctuations in the longitudinal component of the air velocity. They found that the propagation velocity of the pressure disturbances in a shearing flow was equal to that of the velocity fluctuations. Furthermore, the space–time correlation functions between pressure and velocity were quite similar in shape and scale to those of the component of turbulent velocity, u'. These conclusions have been placed on a more theoretical foundation recently

by Bradshaw (1967). Relying on arguments that the large eddies of the turbulence are axisymmetric, Bradshaw deduced that the pressure spectrum and the $\overline{(u')^2}$ spectrum in the outer portion of the boundary layer should be identical at low frequencies. Consequently, a study of the low-frequency end of the u' intensity spectrum should yield information on the pressure fluctuation at corresponding frequencies. Since most of the energy of the spectrum is associated with low

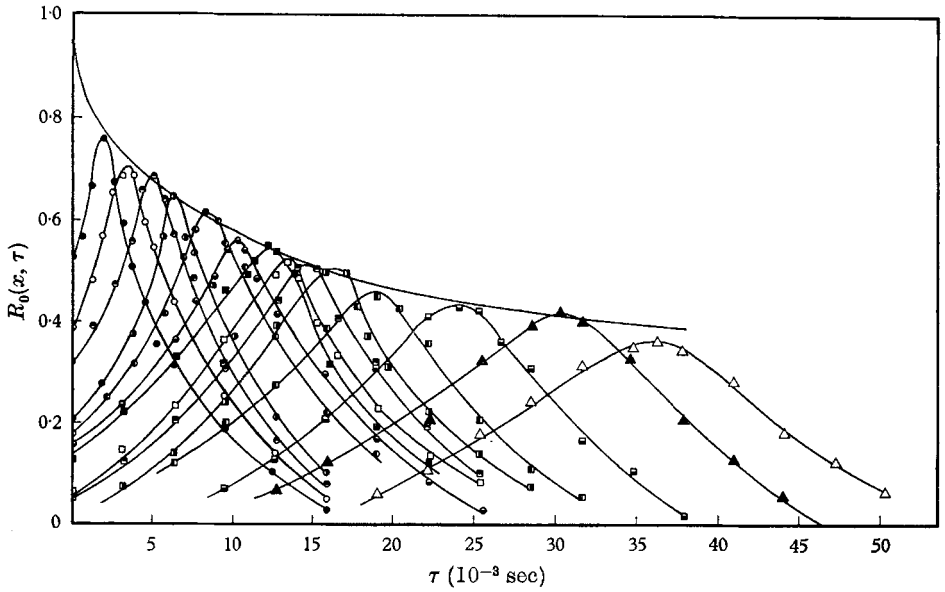

FIGURE 15. Space–time correlations for the longitudinal component of air turbulence, where $u_* = 35$ cm sec^{-1}, and the distance above the mean water level is $y = 2{\cdot}5$ cm. Fixed probe 12·7 cm upstream from leading edge. $u_* = 37$ cm sec^{-1}, $y = 2{\cdot}5$ cm.

x cm		x cm
●	1·27	□ 10·16
○	2·54	▫ 11·43
◓	3·81	◨ 12·70
◑	5·08	◧ 15·24
◐	6·35	▫ 20·32
◒	7·62	▲ 25·40
■	8·89	△ 30·48

frequencies, the average progression velocity of the spectrum is governed by the average progression velocity of the low-frequency components. Thus, measurements of the average progression velocity of the turbulence intensity pattern can be interpreted in terms of the mean progression velocity of the low-frequency fluctuation in pressure.

We therefore, designed an additional experiment to check indirectly for the possibility of finding low-frequency pressure waves moving at the phase velocity of observed modes of the surface waves. It consisted of measuring the progression velocity of the u' intensity pattern from space–time correlations such as the example shown in figure 15. To obtain these curves, a hot-wire probe was embedded into the aluminium plate 12·7 cm upstream of the beginning of the water

surface and was elevated to 2·5 cm in the approaching air stream and thus extended well into the outer portion of the boundary layer. At the same elevation, but downward from this fixed probe, a movable probe was located at various distances such that the distance (x) between the two probes was varied from 2 to 30 cm. At a given probe spacing, the two hot-wire signals were recorded simultaneously on the FM tape recorder. The space–time correlations were calculated by analogue techniques using the relation

$$R_0(\tau, x) = \frac{1}{\overline{u'^2} T} \int_0^T u'(t, x_0)\, u'(t+\tau, x_0+x)\, dt, \tag{10}$$

where x_0 is the location of the fixed probe, τ is the delay time of one signal with regard to the other, and T is the averaging (sampling) time.

From the space-time correlations a curve of the progression velocity u_p is found by plotting the delay time τ_p corresponding to the peak correlation *vs.* distance x, and determining u_p locally by the definition $u_p = dx/dt_p$. The progression velocity was found to be constant and about equal to $0{\cdot}8\,u_\infty$ ($8{\cdot}5$ m sec^{-1}), which is well above the phase velocity of any observed waves.

From the data in figure 15, we note that the turbulent flow pattern is quite persistent. At a distance x of 30 cm, the maximum correlation coefficient had only dropped to 0·4, which should give the pressure pattern sufficient coherence to raise waves, but, because of its high progression velocity, the oscillatory pressure pattern could feed energy only to waves which travel obliquely to the direction of mean air flow, with resonance occurring when the angle between the direction of propagation of the waves and the wind direction is given by $\cos\alpha = c/u_p$ (Phillips 1957). This requires angles between wave crest and wind direction in this study of between 0 and 10°, which were not observed. Even the smallest capillary ripples of wavelength about 0·5 cm have a phase velocity of only 30 cm sec^{-1} and thus, for the lowest air velocity at which waves were observed (critical fetch at $x = 4{\cdot}88$ m), one should have found the smallest value $\alpha = 78°$.

Our experiments have thus yielded no evidence which can be used for support of existing theories on the inception of the very first ripples. They have, however, brought out some facts which were not observed before, such as the dependency of the frequency of the first waves on the surface shear stress, which will have to be explained by future models of generation of water surface waves on smooth water.

4.3. *Shearing flow instability*

Once the initial disturbances exist, regardless of their origins, energy can be transferred to them by the viscous mechanism described by Benjamin (1959) and Miles (1962*a*). Assuming that this mechanism controls further growth of the first wavelets, it will be active at all fetches in the first two stages of growth as we have defined them, and to some extent also in the third stage.

The analytical solution of Miles (1962*a*) applies to conditions of a logarithmic distribution of air velocity that does not change with fetch. Furthermore, no mean velocity gradient is accounted for in the water. The waves of wave-number k are assumed infinitesimal in amplitude a ($ak \ll 1$), and the critical layer, where

$u(y) = c$, is presumed to lie within the viscous sublayer of the air flow. The model of Miles is valid if

$$c_0 < 2{\cdot}3(u_*/\nu_a k)^{\frac{1}{3}} u_*, \tag{11}$$

where the phase speed c_0 is given by

$$c_0 = \left[\frac{g}{k} + \frac{k\gamma}{\rho_w}\right]^{\frac{1}{2}}. \tag{12}$$

Here γ is the surface tension between air and water. These restrictions, with the exception of zero velocity in the water, were fulfilled within the first 50 cm downstream of the plate, in our experiments involving the high wind speed and over some distance upstream and downstream of the critical fetch in the case of the low wind speeds.

The linearized stability theory of Benjamin and Miles traces the development of small disturbances of the type

$$\eta = a_0 \exp\left[ik(x - ct)\right], \tag{13}$$

where η is the water surface displacement, a_0 is the amplitude of the initial disturbance of wave-number k, and c is its complex phase speed given as

$$c = c_0 + ic_i. \tag{14}$$

Disturbances will grow if the imaginary part c_i is positive. The net amplification factor $m = kc_i$ consists of a sum of two terms: a growth rate m_a due to the Miles–Benjamin mechanism, and a damping rate m_w resulting from viscous dissipation of wave energy in the water. From the theory of small-amplitude waves

$$m_w = -2k^2\nu_w - (2k^3\nu_w c_0)^{\frac{1}{2}} \exp(-2kd), \tag{15}$$

where d is the depth and ν_w is the kinematic viscosity of the water. The phase speed c_0 of the infinitesimal waves is assumed unaffected by the process of energy transfer from the air to the water. The growth factor is determined from a solution of the viscous Orr–Sommerfeld equation as (Miles 1962*a*)

$$m_a = \frac{1}{2}\left(\frac{\rho_a}{\rho_w}\right) U_0' \left[\frac{w_i - F_i - k\delta^*(w_r - F_r)\, H_i}{|F - w|^2}\right]_{c=c_0}, \tag{16}$$

where F and H are complex functions of the variable

$$Z = c/U_0'\delta^* \tag{17}$$

and w is a complex function discussed by Miles (1962*b*).

Since it is assumed that the velocity profile nearest the water is linear, the slope U_0' of the mean wind profile at the surface is given by

$$U_0' \approx u_*^2/\nu_a.$$

The parameter δ^* is given by $(\nu_a/U_0' k)^{\frac{1}{2}}$. In Miles' (1962*a*) approximations, $w_i = 0$ so that

$$|F - w|^2 = (F_r - w_r)^2 + F_i^2. \tag{18}$$

In our calculations for m_a, F_r, F_i and H_i were determined from curves given in figure 3 of Miles (1962*a*) paper. The w function was estimated from Miles (1962*b*), where

$$w = \frac{\kappa c_0}{u_*} W(R, A), \quad R = \frac{\kappa u_*}{k\nu_a} \quad \text{and} \quad A = \frac{\kappa(u_1 - c_0)}{u_*}.$$

The velocity u_1 at the edge $y = y_1$ of the viscous sublayer is found from the condition that the logarithmic law in the form given by Miles (1962*a*)

$$u(y) = u_1 + \frac{u_*}{\kappa}\left[\ln\left(\frac{4\kappa u_* y}{\nu_a}\right) - 1 + O(y_1/y)\right] \tag{19}$$

must asymptotically approach (2) for large values of y. With the term

$$O[y_1/y] \approx 0$$

in Miles' equations, it follows that

$$\frac{u_1}{u_*} \approx 6{\cdot}9. \tag{20}$$

This value is within the range of 5·6 to 8 used in Miles' calculations.

From the above equations, the theoretical amplification factors m_a and m_w were calculated for the experimental conditions of this study. We note that the only wave component to which the Miles' model applies without ambiguity is that corresponding to the peak of the spectrum; i.e. to the dominant wave. On this we shall therefore concentrate. To extend the results to the whole spectrum requires superposition of solutions, which is possible in principle because of the linearity of the model. Other wave components than the peak, however, are more likely to be affected by disturbances in the velocity profiles due to the dominant component. The results for spatial growth of the dominant waves have already been introduced in figure 13. The theory of Miles' yields growth rates in time, which have to be converted to spatial rates by means of the transformation (Gaster 1962)

$$S_T = \frac{\partial \ln \phi(n)}{\partial x} = \frac{2m}{c_g}, \tag{21}$$

where $m = m_a + m_w$ from (15) and (16), and c_g is the group velocity:

$$c_g = c_0\left[1 - \frac{1}{2}\left(\frac{\rho_w - k^2\nu}{\rho_w + k^2\nu}\right)\right], \tag{22}$$

where ρ_w is the water density.

The theoretical slope S_T then can be compared with the slope S_E obtained from experimental data. S_E was determined as the slope of the best-fitting straight line passing through a plot of $\log \phi(n)$ *vs.* x. This slope is equal to twice the growth rate of the wave amplitude, since the spectrum corresponds to the wave amplitude squared. A comparison of data based on theory and experiment is given in table 4. These results indicate fractional differences of 61 % or less between theory and experiment for growth of the dominant waves in the second stage of development. In two of the four cases listed the difference is outside the estimated uncertainty in evaluating the slope S_E.

All of the data listed in table 4 coincided with Miles' (1962*a*) additional restriction that the ratio $[(\rho_a/\rho_w)u_*^2/\nu_a k] < c_0$. When these two velocity scales become of the same order, the growth rates of small waves may be modified by the Kelvin–Helmholtz class of instability.

Because of the sharpness of the spectral peaks, caution has to be used in interpreting the growth of Fourier components on either side of the spectral peak. However, it is useful for a qualitative comparison to examine the experimental slope along with the theoretical values over a range of wave-numbers. As an

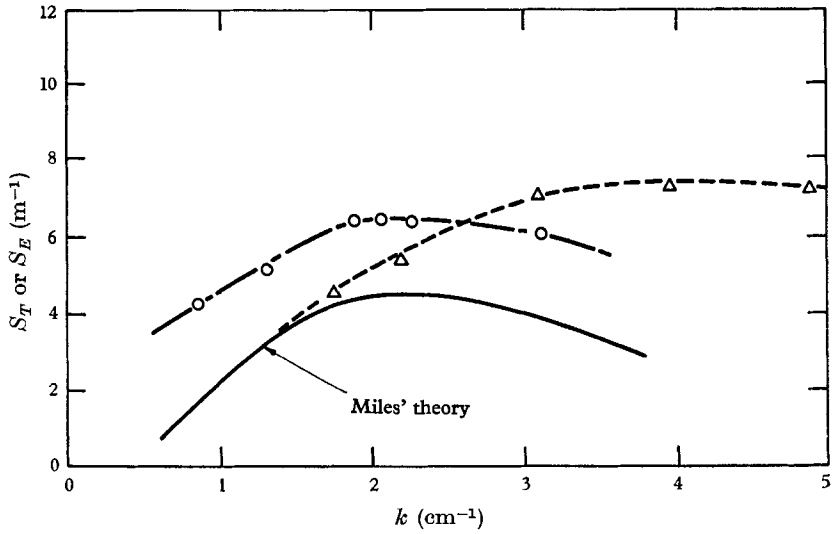

FIGURE 16. Comparison between experimental results and Miles' (1962*a*, *b*) theory, with Drake's (1967) theory correcting for the drift current. The wave-number for the experimental data has been modified for water surface speed by (23). ○, experiment; △, Drake's theory.

illustration of the distribution of the amplification factor in terms of the slope S, theoretical and experimental results for $u_* = 19$ cm sec^{-1} are plotted together in figure 16.

The influence of the surface current. One potentially serious limitation of Miles' theory is the disregard for the shearing current that develops in the water. Taking this motion into account might improve the predictions of the two-dimensional theory for shearing flow instability.

Since our measurements are taken at a fixed location, two possible effects of the current may enter into the comparison between theory and experiment. The first involves accounting for a shift resulting from the finite surface velocity, u_s, on the transformation between wave-number and frequency. The second influence may stem from the fact that the gradients in the drift current in the thin viscous layer at the water surface may modify the growth rates as well as the dissipation rates. An increase in amplitude may be expected by increased energy transfer to the water associated with the surface current, as has been illustrated by Tominaga (1964) for the case of waves on a current of uniform velocity. This is partially compensated for by an increase of the dissipation rate.

To examine the importance of the drift current on our wave measurements, we looked at instability theories that attempted to incorporate such an effect. Miles' mechanism has been applied to superimposed liquids with linear velocity profiles by Feldman (1957) and Miles (1960). However, Miles' and Feldman's models differ from our laboratory condition by the assumption that the critical layer was supposed to exist in the lower, heavier fluid.

u_* (cm sec^{-1})	n_{max} (Hz)	k (cm^{-1})	c_0 (cm sec^{-1})	$\frac{\rho_a u_*^2}{\rho_w \nu_a k}$ (cm sec^{-1})	z
15·8	7·0	1·64	26·7	0·84	0·451
17·0	7·5	1·82	25·9	0·87	0·417
19·0	8·5	2·16	24·7	0·91	0·362
35·0	11·0	2·96	23·4	2·54	0·167

m_a (sec^{-1})	$-m_w$ (sec^{-1})	$\frac{2mx}{c_g}$	S_T (m^{-1})	S_E (m^{-1})	% diff. $\frac{(S_T-S_E)100}{S_E}$
0·241	0·054	13·4	2·1	1·3 ± 0·4	+61
0·354	0·066	15·4	3·1	3·7 ± 0·8	−16
0·497	0·0933	21	4·3	6·5 ± 0·6	−34
2·57	0·175	2·18	24	25 ± 1	− 4·0

TABLE 4. Comparison between experimental growth of dominant wave with fetch and Miles' theoretical predictions assuming $u_1 = 6{\cdot}9u_*$.

A model in which the critical layer lies in the air and in which velocity gradients exist in both fluids has been considered for gas flow over thin liquid layer by Cohen & Hanratty (1965). A newer theory for deeper liquid layers has been reported by Drake (1967), and by Drake & Plate (1968). This model is adopted here to predict the behaviour of waves in the second stage of growth. The application of this model requires that the water surface velocity be known in addition to the parameters of Miles' model. We used the experimental results for the water surface velocity reproduced in figure 14.

Drake's model assumes a mean velocity distribution which is identical in the air with that of Miles (1962*a*) with the exception of accounting for translation due to the surface velocity. To specify the water current, a linear profile in the thin layer near the water surface is assumed which abruptly changes with depth into a logarithmic profile fixed at the bottom of the channel. For deep water waves, the contribution from the logarithmic portion of the current profile to energy transfer becomes unimportant. Thus the linear profile, which originally was developed for instabilities of small disturbances on a moving stream, can be applied readily to wave growth in the case of a shear-induced current in water standing in the channel. To a first approximation, the following equation for the phase speed, $c_r - u_s$, relative to the surface velocity is found (Drake 1967):

$$(c_r - u_s)^2 + \frac{u_*^2 \rho_a}{\mu_w k}(c_r - u_s) - c_0^2 \approx 0, \tag{23}$$

where μ_w is the viscosity of water.

To higher approximations, the right side of (23) is equal to the complex function $u_*^2 Q$, where Q is given by

$$-Q = \frac{G_w + G_a}{1 + F_w + F_a}. \tag{24}$$

In this equation, the functions with subscript w stem from the water solutions of the Orr–Sommerfield problem, while G_a and F_a result from the air motion.

These functions are given by Drake & Plate (1968) in terms of c_r, u_* and u_s. A solution for (23) and (24) is obtained iteratively by assuming first $Q = 0$, calculating c_r from (24) and inserting this value into the terms for the functions G and F in (24), from which a new estimate for Q is found. The new approximation for Q

u_* (cm sec^{-1})	u_s (cm sec^{-1})	$n_{\max}$ (Hz)	k(corr.) (cm^{-1})	S_T (m^{-1})	S_E (m^{-1})	$\frac{(S_T - S_E)\,100}{S_E}$
15·8	8·90	7·0	1·36	2·0	1·3 ± 0·4	+54
17·0	9·75	7·5	1·59	3·1	3·7 ± 0·8	−16
19·0	10·7	8·5	1·91	5·1	6·5 ± 0·6	−22

TABLE 5. Comparison between experimental growth of dominant wave with fetch and Drake's theory accounting for the effect of the drift current $u_1 = 6{\cdot}9u_*$.

results in a revised complex phase velocity $c - u_s$. The iteration is repeated until a constant value of c is attained whose imaginary part is converted into the spatial growth rate by means of (21) from the time growth rates $m = kc_i$, with c given by (23).

For the spectral wave peaks observed at low shearing velocities, calculations of the growth rates in terms of S_T from Drake's model are compared with experimental results in table 5. For these calculations, u_s was taken as $u_s = 0{\cdot}026\,u_\infty$. The incorporation of the influence of the drift current evidently slightly improved the agreement between theory and experiment, particularly in the $u_* = 19$ cm sec^{-1} case, for the dominant waves in stage two of growth.

To illustrate differences and similarities of Drake's and Miles' models, the case of $u_* = 19$ cm sec^{-1} was used again as is shown in figure 16. At low wave-numbers, $k < 1$ cm^{-1}, both models give essentially the same results for S_T. For larger wave-numbers, however, Miles' theory predicts lower growth rates than Drake's model with a maximum at $k \approx 2{\cdot}3$ cm^{-1}. On the other hand, Drake's model shows a nearly constant rate of growth with fetch beyond a wave-number of about 3 cm^{-1}.

A comparison of the shape of the growth rate function shows that the experimental curve obtained from all spectral components of the spectrum for $u_* = 19$ cm/sec agrees more closely with that obtained from Miles' theory than that from Drake's theory. It is not clear whether this result is of any significance, since frequency components [of the spectrum] other than the dominant are perhaps not really growing as indicated in the spectrum. The spectral peaks observed at a given u_* are actually systematically higher than those predicted by Miles' theory as indicated in table 3, even though it predicts correctly the

decrease with decrease in wind speed of the frequency associated with the peak. In contrast to those results, it is found that Drake's model slightly improves the estimate of the growth rate, but it fails to yield any frequency component which grows faster than all others. The conclusion to be derived from these observations is that presently existing models fail to predict growth rates which are in perfect agreement with experiments. We believe that our experiments are sufficiently accurate, and that the discrepancies between experiments and theory must be attributed to the latter itself, or to its interpretation.

We are indebted to C. L. Liu, K. S. Su, J. R. Lai and R. Biro for the assistance in data processing. The helpful comments of J. W. Deardorff in revising the original manuscript are greatly appreciated. This work was sponsored by the National Science Foundation in connexion with its contract with the National Center for Atmospheric Research, and its grant no. GK 188 to Colorado State University.

Appendix

The equation for the equilibrium range of water wave spectra had been derived by Phillips (1958) with the notion of defining the high-frequency end of the spectrum. The resulting law (9) is, however, found to be in much better agreement with the envelope to the high-frequency end of all existing water surface spectra than with the high-frequency end of individual spectra. We think that this indicates that only the dominant wave of the spectrum, rather than all high-frequency wave components, has reached a limiting amplitude which is bounded by (9). In fact, the law (9) can be derived for the spectral peaks without any assumption on the shape of the spectrum except that it is universal—an assumption that was made by Hidy & Plate (1965), who proposed a universal spectral shape presented by plotting

$$S\left(\frac{n}{n_{\max}}\right) = \phi(n)\frac{n_{\max}}{\sigma^2} \tag{A 1}$$

versus $n/n_{\max}$, where S is the dimensionless spectral function and σ^2 is the variance of the water surface elevation.

Let the water surface perturbation have a peaked spectrum, i.e. consist of a dominant wave with frequency $n_{\max}$ whose amplitude is modulated by a random function. Then it can be assumed that the amplitude of the dominant wave is limited by gravity. To be specific, we assume that the maximum acceleration $a_{\max}$ of the average of the highest third of the waves is proportional to g. If the average wave height is denoted by $H^{(\frac{1}{3})}$, then this assumption yields

$$\alpha g = a_{\max} = \frac{H^{(\frac{1}{3})}}{2}(2\pi n_{\max})^2, \tag{A 2}$$

where α is a factor of proportionality which presumably should lie around 0·5, the limiting value corresponding to the Stokes finite-amplitude wave.

According to Longuet-Higgins (1952), the wave heights of such a record have a Rayleigh probability distribution, for which one obtains for a Gaussian surface

$$\sigma^2 = \tfrac{1}{16}[H^{(\frac{1}{3})}]^2, \tag{A 3}$$

and consequently, with (A 2),

$$\sigma^2 = \tfrac{1}{4}\alpha^2 g^2 (2\pi n_{\max})^{-4}. \tag{A 4}$$

From the results of Hidy & Plate (1965) it is found that for the similarity spectrum

$$S(1) = \phi(n_{\max})\frac{n_{\max}}{\sigma^2} \approx 0{\cdot}5. \tag{A 5}$$

Consequently one obtains from (A 4) and (A 5)

$$\phi(n_{\max}) = \frac{\alpha^2 g^2}{8(2\pi)^4} n_{\max}^{-5}. \tag{A 6}$$

A comparison of (9) and (A 6) shows that

$$\beta = \alpha^2/8(2\pi)^4.$$

If this value is compared with the value $\beta = 7{\cdot}5 \times 10^{-6}$ found by Phillips (1966) from many different spectra, then it is seen that $\alpha = 0{\cdot}29$, which is of the expected order of magnitude.

REFERENCES

Benjamin, T. B. 1959 *J. Fluid Mech.* **6**, 161.

Blackman, R. B. & Tukey, J. W. 1958 *Measurements of Power Spectra from the Point of View of Communications Engineering*. New York: Dover.

Bradshaw, P. 1967 *J. Fluid Mech.* **27**, 209.

Clauser, F. 1956 The turbulent boundary layer. *Adv. Appl. Mech.* **4**. New York: Academic Press.

Cohen, L. S. & Hanratty, T. J. 1965 *A.I.Ch.E. J.* **11**, 138.

Drake, R. 1967 The generation of wind waves on open channel flows. Unpublished Ph.D. dissertation, Colorado State University, Department of Civil Engineering, Fort Collins, Colorado.

Drake, R. & Plate, E. J. 1968 The generation of wind waves on open channel flows. *Proc. 10th Midwestern Mechanics Conference.*

Feldman, S. 1957 *J. Fluid Mech.* **2**, 343.

Gaster, M. 1962 *J. Fluid Mech.* **14**, 222.

Hess, G. D. 1968 Turbulent air flow over small water wave. Unpublished Ph.D. dissertation, University of Washington, Seattle, Washington.

Hidy, G. M. & Plate, E. J. 1965 *Phys. Fluids*, **8**, 1387.

Hidy, G. M. & Plate, E. J. 1966 *J. Fluid Mech.* **26**, 651.

Hinze, J. O. 1959 *Turbulence*. New York: McGraw-Hill.

Keulegan, G. H. 1951 *J. Natl Bur. of Standards*, **46**, 358.

Klebanoff, P. S. 1954 *NACA T.N.* 3133.

Laufer, J. 1954 *NACA T.R.* 1174.

Longuet-Higgins, M. S. 1952 *J. Marine Res.* **11**, 245.

Miles, J. W. 1960 *J. Fluid Mech.* **8**, 593.

Miles, J. W. 1962*a* *J. Fluid Mech.* **13**, 433.

Miles, J. W. 1962*b* *J. Fluid Mech.* **13**, 427.

PHILLIPS, O. M. 1957 *J. Fluid Mech.* **2**, 417.

PHILLIPS, O. M. 1958 *J. Fluid Mech.* **4**, 426.

PHILLIPS, O. M. 1966 *The Dynamics of the Upper Ocean.* Cambridge University Press.

PLATE, E. J. 1965 *La Houille Blanche*, no. 6, 595.

PLATE, E. J. & HIDY, G. M. 1967 *J. Geophys. Res.* **72**, 4627.

POND, S., STEWART, R. W. & BURLING, R. W. 1963 *J. Atmos. Sci.* **20**, 319.

SANDBORN, V. A. & MARSHALL, R. D. 1965 *Local Isotropy in Wind Turbulence.* TR CER-65VAS-RDM71, Civil Engineering Department, Colorado State University, Fort Collins, Colorado.

SUTHERLAND, A. 1967 *Spectral Measurements and Growth of Wind-generated Water Waves.* TR 84, Department of Civil Engineering, Stanford University, Stanford, California.

TOMINAGA, M. 1964 *Bull. Soc. Franco-Japonaise d'Oceanographie*, **2**, 22.

WILLMARTH, W. & WOOLDRIDGE, C. 1962 *J. Fluid Mech.* **14**, 187.

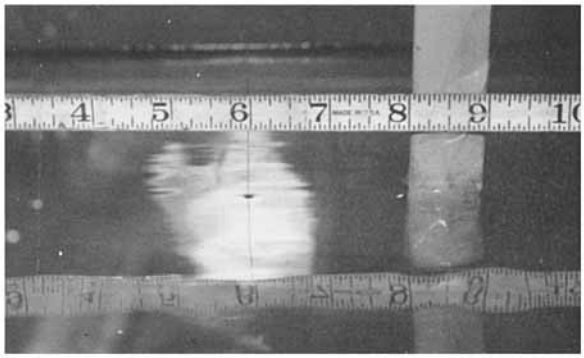

(*a*)

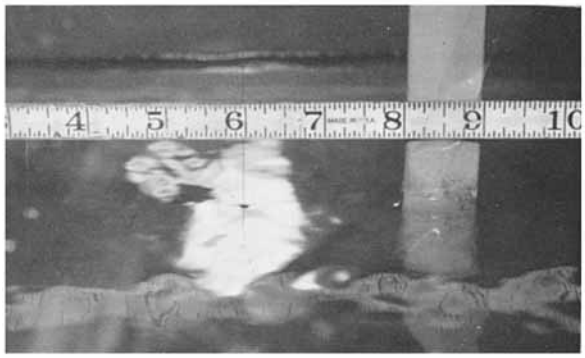

(*b*)

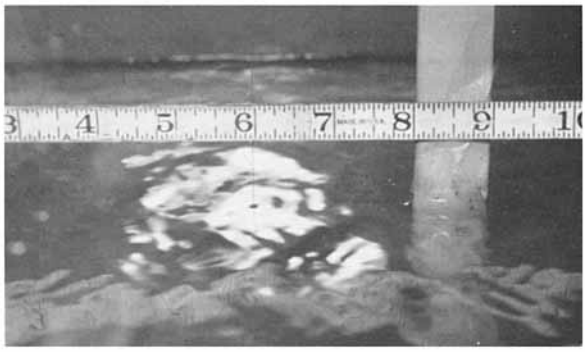

(*c*)

FIGURE 2. Photographs of reflexions of the capacitance gauge wire on the water surface. Scale is shown in inches.

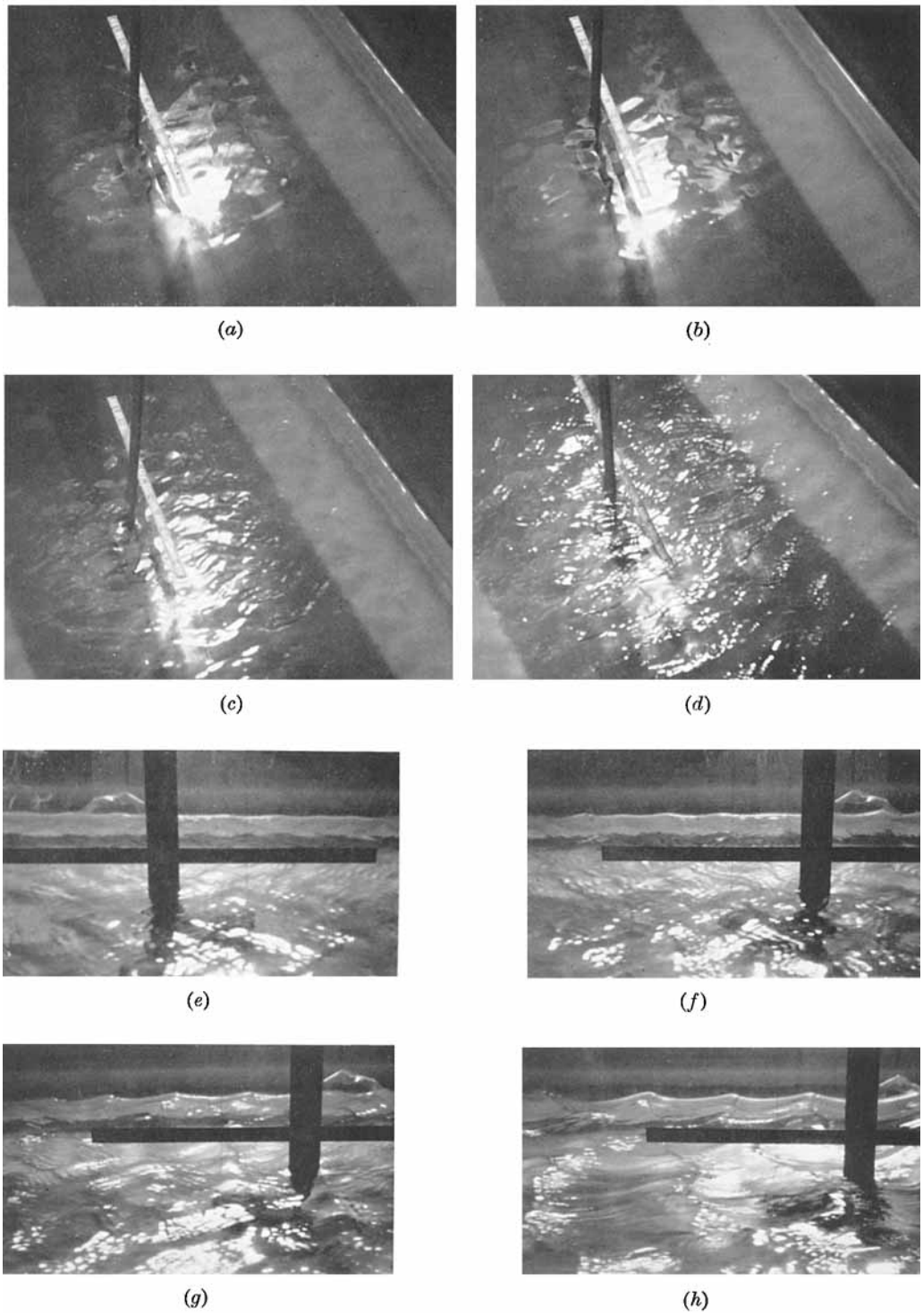

FIGURE 8. Photographs of the onset of visible surface waves at the critical wind speed with inlet grid for fetch $x = 3{\cdot}5$ m. The ruler measures distance x in inches. Three-quarter views down tunnel: (*a*) just below critical speed, $u_\infty = 2{\cdot}9$ m sec^{-1}; (*b*) just above critical speed, $u_\infty = 3.1$ m sec^{-1}; (*c*) at higher wind speed, $u_\infty = 3{\cdot}4$ m sec^{-1}; (*d*) still higher wind speed, $u_\infty = 4{\cdot}2$ m sec^{-1}. Views from side of tunnel: (*e*) $u_\infty = 3{\cdot}8$ m sec^{-1}; (*f*) $u_\infty = 4{\cdot}3$ m sec^{-1}; (*g*) $u_\infty = 5{\cdot}3$ m sec^{-1}; (*h*) $u_\infty = 7{\cdot}5$ m sec^{-1}.

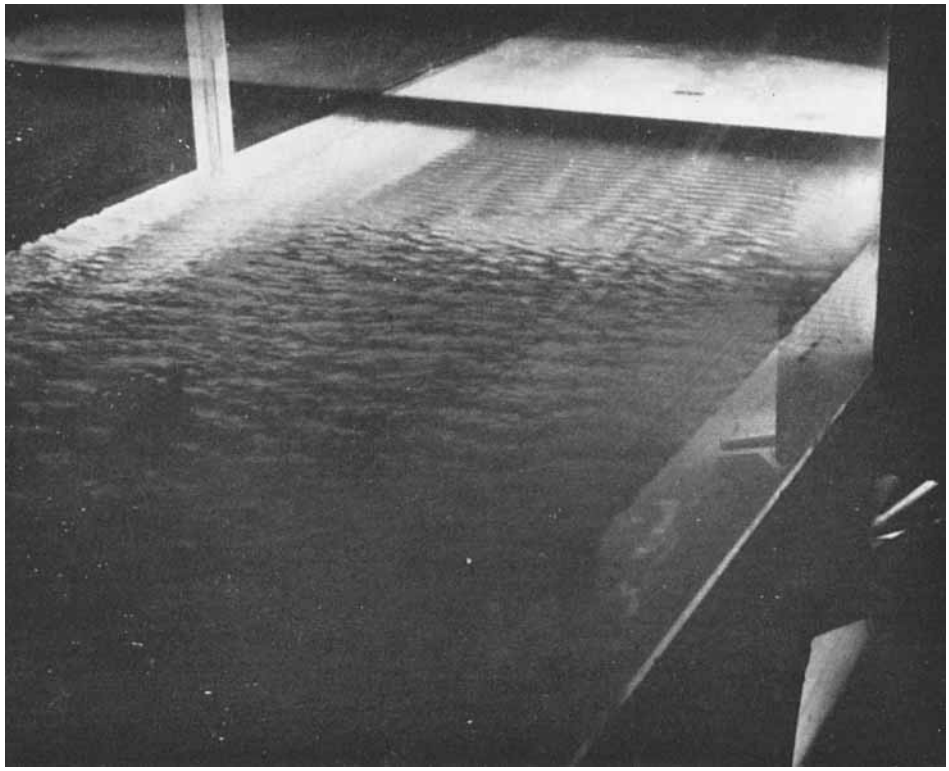

FIGURE 9. Photograph of waves on the water taken near the trailing edge of the aluminium plate for $u_* = 35$ cm sec^{-1}.